Research Square

Preprints are preliminary reports that have not undergone peer review.
They should not be considered conclusive, used to inform clinical practice,
or referenced by the media as validated information.

Lambert-W Spectral Deflation with Tight-Frame Least Squares for Retarded Delay Differential Equations

Mutaz Mohammad

Mutaz.Mohammad@zu.ac.ae

Zayed University

Research Article

Keywords: delay differential equation, Lambert W function, spectral deflation, pole cancellation, tight framelets, B-splines, least squares, long-time integration, stability

Posted Date: November 4th, 2026

DOI: https://doi.org/10.21203/rs.3.rs-11283145/v1

License: This work is licensed under a Creative Commons Attribution 4.0 International License.
Read Full License

Additional Declarations: No competing interests reported.

Lambert-W Spectral Deflation with Tight-Frame Least Squares for Retarded Delay Differential Equations

Mutaz Mohammad[1,*]

[1]Department of Mathematics, Zayed University, Abu Dhabi, United Arab Emirates

Corresponding author*: Mutaz.Mohammad@zu.ac.ae

Abstract

Scalar retarded delay differential equations are infinite-dimensional even when their coefficients are constant, because the characteristic equation contains infinitely many roots. This paper develops a hybrid approximation in which the slowly decaying characteristic content is removed analytically before a localized numerical discretization is applied. For

$$u'(t) = au(t) + bu(t-\tau) + g(t), \qquad u(t) = \phi(t) \text{ for } -\tau \le t \le 0,$$

the characteristic roots are represented by Lambert-W branches. Exact residues associated with selected simple roots are used to cancel those poles, leaving a residual DDE with a modified history but the same differential operator. Three analytical results support the construction. First, finite modal deflation is shown to cancel the selected Laplace poles exactly. Second, under an explicit contour-shift hypothesis, the residual decays at any exponential rate to the right of the first nondeflated spectral abscissa. Third, after the prescribed history is separated from the unknown, the least-squares operator satisfies a finite-horizon coercivity estimate in H^1, which yields quasi-optimality and an a posteriori residual bound. The residual is discretized in a redundant piecewise-linear B-spline framelet dictionary generated by the unitary extension principle, with the linear system solved by a rank-revealing least-squares factorization. A manufactured solution gives essentially second-order maximum and RMS convergence. For the weakly damped problem $u' = -u - 2u(t-1)$, at the same effective dimension 257, dominant-pair deflation reduces the maximum error on $[0, 8]$ from 2.46×10^{-3} to 7.19×10^{-4} and the RMS error from 1.40×10^{-3} to 1.45×10^{-4}. Deflating additional, more oscillatory pairs at the same resolution is less accurate, which motivates a resolution-aware mode-selection rule based on the computable residual. For a final horizon $T = 50$, solving the numerical residual only to $T_w = 8$ and then retaining the dominant Lambert pair gives a global maximum error 7.18×10^{-4}, while the omitted tail after T_w is below 1.67×10^{-6}. The main benefit is therefore not matrix conditioning, which is unchanged for a fixed frame space, but accuracy per degree of freedom and a long-time representation whose numerical part can be confined to the transient window.

Keywords: delay differential equation; Lambert W function; spectral deflation; pole cancellation; tight framelets; B-splines; least squares; long-time integration; stability.
MSC 2020: 34K06, 34K20, 65L03, 65L10, 42C40.

1 Introduction

Delay differential equations (DDEs) retain a segment of the past state, so a scalar equation evolves on a function space rather than on a finite-dimensional state space. The numerical consequences are familiar but important: nonsmoothness in the history can propagate through successive delay intervals, stability depends on an infinite characteristic spectrum, and methods designed for ordinary differential equations require delay-aware interpolation and discontinuity handling. Classical analysis and numerical foundations are developed in the monographs of Hale

and Verduyn Lunel [1] and Bellen and Zennaro [2]. Practical method-of-steps solvers based on continuous Runge-Kutta formulas, including the algorithm underlying `dde23`, remain a standard reference point [3].

For the scalar single-delay equation with constant coefficients, the transcendental characteristic equation has a special structure. Its roots can be written exactly in terms of the branches of the Lambert W function, whose analytic properties were systematized by Corless et al. [4]. Asl and Ulsoy used Lambert-W representations in the analysis of linear delay systems [5], and Yi, Nelson, and Ulsoy developed the approach further for analysis and control [6]. The scalar formula is unambiguous, but extensions to multidimensional systems require care. Hwang and Cheng identified pitfalls in branch-based stability calculations [7], Jarlebring and Damm proved explicit spectral formulas under simultaneous triangularizability [8], and Cepeda-Gomez and Michiels showed that matrix Lambert branches do not, in general, have a one-to-one correspondence with characteristic roots [9]. Generalized Lambert functions have also been used for neutral equations [20], and Lambert-based qualitative analysis has recently been extended to fractional delay problems [21].

Numerical work on DDEs has developed along a different axis. Pseudospectral discretizations approximate characteristic roots and stability information efficiently [10], while recent spectral collocation methods use multidomain constructions to resolve delay-propagated loss of smoothness [12]. Pseudospectral ideas also support stability and bifurcation analysis for equations with infinite delay [11].

Wavelet and frame constructions offer another route because compact support and multiresolution are naturally suited to localized irregularity. Tight wavelet-frame discretizations have also been developed for nonlinear fractional differential equations, including fractional Riccati problems [15]. For delay equations specifically, Euler-wavelet collocation has been used for neutral DDEs [14], Krawtchouk wavelets for fractional delay equations [16], Haar wavelets for higher-order time-dependent DDEs [17], and a high-order Haar formulation for linear and nonlinear DDEs was reported in 2026 [18]. A fractional Vieta–Lucas wavelet projection method appeared in 2026 [19]. These developments show that localized multiscale discretizations remain active for differential and delay equations, but they also sharpen the novelty requirement: changing the approximation family alone is not sufficient to distinguish a numerical method.

The gap addressed here is more specific. Lambert methods expose a small number of rightmost characteristic modes exactly, while localized discretizations approximate finite-horizon trajectories without using that spectral information. Near weak damping or a stability boundary, a numerical basis may spend many degrees of freedom repeatedly reconstructing a few slowly decaying oscillatory modes that are already known analytically. Conversely, a pure modal truncation is least attractive near the initial time, where history compatibility and step-induced regularity dominate. This suggests a division of labor: represent a small, carefully selected spectral component analytically, then solve only the residual with a local basis. From a numerical viewpoint, the contribution is therefore not the choice of a new approximation family alone, but an algorithm in which analytically accessible dominant delay modes are removed before discretization, thereby changing the spectral content and approximation difficulty of the residual problem.

The paper develops that idea for scalar retarded equations, and it deliberately avoids two claims that would be difficult to defend. First, the Lambert representation itself is not new. Second, for a fixed numerical space, subtracting modes does not change the least-squares matrix, so it is not a matrix preconditioner and does not improve its singular-value condition number. The gain is approximation-theoretic: the right-hand side and residual history are changed so that the local basis resolves a smaller long-time component. This distinction is confirmed numerically in section 7.

The contribution of this work is built around a simple idea, namely, to remove analytically the dominant delay modes before approximating the remaining transient numerically. For a

general prescribed history, we derive the residue associated with each simple Lambert root and show that subtracting a finite set of modal contributions cancels the corresponding poles of the transformed solution exactly. Under the stated inverse-Laplace contour assumption, this leads to a spectral-gap result showing that the deflated residual is governed asymptotically by the first root that has not been removed. This provides a direct justification for the long-time strategy adopted later, where the numerical approximation is restricted to the transient interval and the analytically extracted modes are used to represent the solution beyond that window.

The numerical treatment is developed around this residual formulation. The prescribed history is separated from the unknown trajectory so that the finite-horizon operator is genuinely linear in the quantity being approximated. This makes it possible to derive an explicit H^1 stability estimate, followed by a least-squares quasi-optimality result and a residual-based a posteriori error bound. The approximation itself is constructed from compactly supported piecewise-linear B-spline tight frames following the framework of Daubechies, Han, Ron, and Shen [13]. Since restricting the frame system to a bounded interval produces a redundant dictionary, the resulting discrete system is solved through a rank-revealing least-squares procedure rather than by assuming linear independence of the basis functions.

An additional point that becomes important in practice is the choice of how many Lambert modes should be removed. More deflation is not necessarily better at a fixed resolution, because higher branches introduce increasingly oscillatory components into the residual history. For this reason, the number of deflated modes is selected through the computed least-squares residual rather than by prescribing a fixed branch count in advance. The numerical experiments are designed to examine these issues separately. A manufactured solution is used to check the convergence of the frame discretization, a weakly damped example compares the direct and deflated formulations under the same numerical resolution, and a long-time experiment tests the transient-windowing strategy. A final Hopf-type example is included to confirm that the relevant Lambert branches recover the expected stability transition. The resulting computational sequence, including factorization reuse and residual-based mode selection, is summarized in algorithm 1.

The present analysis is deliberately restricted to a scalar retarded equation with a single discrete delay. In this setting, the characteristic roots are available explicitly through the branches of the Lambert W function, so the spectral part of the deflation can be studied without introducing an additional approximation. For systems, multiple delays, or neutral equations, the same principle may still be useful, but the spectral representation and the deflation step require a different treatment. These extensions are therefore left for future work.

2 Problem class, well-posedness, and transformed representation

We consider

$$u'(t) = au(t) + bu(t-\tau) + g(t), \qquad 0 < t \le T, \tag{2.1}$$

$$u(t) = \phi(t), \qquad -\tau \le t \le 0, \tag{2.2}$$

where $a, b \in \mathbb{R}$, $\tau > 0$, $T > 0$, $\phi \in C([-\tau, 0])$, and $g \in L^1_{\mathrm{loc}}([0, T])$. When H^1 estimates are needed, the data are strengthened accordingly.

Proposition 2.1 (Finite-horizon well-posedness)**.** *If $\phi \in C([-\tau, 0])$ and $g \in L^1(0, T)$, then equations* (2.1) *and* (2.2) *has a unique absolutely continuous solution on every delay interval, hence a unique continuous solution on $[-\tau, T]$ that satisfies equation* (2.1) *almost everywhere.*

Proof. On $0 \le t \le \min\{\tau, T\}$, the delayed value is prescribed by the history, and

$$u'(t) - au(t) = b\phi(t-\tau) + g(t)$$

is a linear ordinary differential equation. It has a unique absolutely continuous solution with $u(0) = \phi(0)$. The solution on this first interval provides the delayed term on the next interval. Repetition of this method-of-steps construction covers $[0, T]$ after finitely many intervals. Uniqueness follows at each step from uniqueness of the corresponding linear ordinary differential equation. □

For the homogeneous spectral analysis, set $g = 0$ and define

$$\Delta(s) = s - a - be^{-s\tau}.$$

When $b \neq 0$, all zeros are

$$\lambda_k = a + \frac{1}{\tau} W_k\big(b\tau e^{-a\tau}\big), \qquad k \in \mathbb{Z}.$$

The formula follows by rewriting $\tau(\lambda - a)e^{\tau(\lambda-a)} = b\tau e^{-a\tau}$. For scalar single-delay equations this branch representation is exact [4, 5].

The derivative of the characteristic function is

$$\Delta'(s) = 1 + b\tau e^{-s\tau}.$$

At a characteristic root,

$$\Delta'(\lambda_k) = 1 + \tau(\lambda_k - a). \tag{2.3}$$

Thus λ_k is simple exactly when the right-hand side of equation (2.3) is nonzero.

Let

$$\Phi(s) = \int_{-\tau}^{0} e^{-s\theta}\phi(\theta)\, \mathrm{d}\theta.$$

If $U(s) = \int_0^\infty e^{-st}u(t)\, \mathrm{d}t$ exists in a right half-plane, then the shifted history gives

$$\int_0^\infty e^{-st}u(t-\tau)\, \mathrm{d}t = e^{-s\tau}\big(U(s) + \Phi(s)\big),$$

and therefore, for the homogeneous equation,

$$U(s) = \frac{N(s)}{\Delta(s)}, \qquad N(s) = \phi(0) + be^{-s\tau}\Phi(s). \tag{2.4}$$

For a simple root λ_k, the associated residue is

$$c_k = \operatorname*{Res}_{s=\lambda_k} U(s) = \frac{\phi(0) + be^{-\lambda_k\tau}\Phi(\lambda_k)}{1 + b\tau e^{-\lambda_k\tau}}. \tag{2.5}$$

This formula is used only for poles that are explicitly extracted. We do not assume, without additional regularity and compatibility hypotheses, that an infinite residue series converges uniformly down to $t = 0$.

2.1 Explicit residues for constant history

A particularly useful case in the computations below is the constant history

$$\phi(t) \equiv 1, \qquad -\tau \leq t \leq 0.$$

In this case, the history transform appearing in equation (2.5) can be evaluated explicitly:

$$\Phi(\lambda) = \int_{-\tau}^{0} e^{-\lambda\theta}\, d\theta = \frac{e^{\lambda\tau} - 1}{\lambda}, \qquad \lambda \neq 0.$$

Consequently, the residue associated with a simple characteristic root λ_k becomes

$$c_k = \frac{1 + be^{-\lambda_k \tau} \dfrac{e^{\lambda_k \tau} - 1}{\lambda_k}}{1 + b\tau e^{-\lambda_k \tau}}.$$

Equivalently,

$$c_k = \frac{1 + \dfrac{b}{\lambda_k}\left(1 - e^{-\lambda_k \tau}\right)}{1 + b\tau e^{-\lambda_k \tau}}. \tag{2.6}$$

For real a, b, and τ, the characteristic roots occur in complex-conjugate pairs. Since the prescribed history is also real, the corresponding residues satisfy

$$c_{\bar{k}} = \overline{c_k}.$$

Hence the contribution of a conjugate pair can be written in the manifestly real form

$$c_k e^{\lambda_k t} + \overline{c_k e^{\lambda_k t}} = 2\,\mathrm{Re}\Big(c_k e^{\lambda_k t}\Big).$$

Writing

$$\lambda_k = \alpha_k + i\omega_k, \qquad c_k = \rho_k e^{i\vartheta_k},$$

gives the equivalent oscillatory representation

$$2\,\mathrm{Re}\Big(c_k e^{\lambda_k t}\Big) = 2\rho_k e^{\alpha_k t}\cos(\omega_k t + \vartheta_k).$$

This form makes explicit the decay rate α_k, angular frequency ω_k, and phase ϑ_k of each extracted Lambert mode. It is also the form used in the numerical experiments when a conjugate pair is deflated.

3 Exact finite spectral deflation

Let $K \subset \mathbb{Z}$ be a finite set of simple characteristic branches and define

$$q_K(t) = \sum_{k \in K} c_k e^{\lambda_k t}, \qquad t \in \mathbb{R},$$

with c_k given by equation (2.5). Since each exponential satisfies the homogeneous DDE for every real t, so does q_K.

Theorem 3.1 (Exact finite deflation and pole cancellation)**.** *Let u solve the homogeneous problem and suppose the transformed representation equation* (2.4) *is valid in a right half-plane. Define*

$$r_K(t) = u(t) - q_K(t), \qquad \psi_K(t) = \phi(t) - q_K(t), \quad -\tau \le t \le 0.$$

Then r_K satisfies

$$r_K'(t) = a r_K(t) + b r_K(t-\tau), \qquad t > 0, \tag{3.1}$$
$$r_K(t) = \psi_K(t), \qquad -\tau \le t \le 0. \tag{3.2}$$

Moreover,

$$R_K(s) = U(s) - \sum_{k \in K} \frac{c_k}{s - \lambda_k} \tag{3.3}$$

has removable singularities at every selected simple pole λ_k, $k \in K$.

Proof. Subtracting the homogeneous equation satisfied by q_K from that satisfied by u yields equation (3.1); subtraction on the history interval gives equation (3.2). The Laplace transform of q_K on $[0,\infty)$ is $\sum_{k\in K} c_k/(s-\lambda_k)$. By definition, c_k is the residue of U at λ_k, so the principal part of U at each selected simple pole is exactly removed in equation (3.3). □

Remark 3.1 (Forced equations). For $g \neq 0$, subtracting any homogeneous q_K still yields a residual with the same forcing g. Pole cancellation of the *full forced transform*, however, requires residues computed from the forced numerator as well. In the numerical method below we use homogeneous deflation to remove slowly damped free modes and leave the external forcing in the residual. We do not claim cancellation of forcing-generated singularities.

3.1 Spectral-gap acceleration

The next result formalizes the long-time effect of exact pole removal. Because inverse-Laplace contour shifts require decay information, the analytic hypothesis is stated explicitly.

Theorem 3.2 (Residual exponential rate)**.** *Let u solve the homogeneous problem, and let R_K be defined by equation* (3.3)*. Assume:*

(H1) all characteristic roots in $\{\operatorname{Re} s > \sigma\}$ are simple and belong to K;

(H2) R_K is analytic in $\{\operatorname{Re} s > \sigma\}$ and has a continuous boundary representation on each vertical line $\operatorname{Re} s = \mu > \sigma$;

(H3) for every such μ, $\omega \mapsto R_K(\mu + i\omega)$ belongs to $L^1(\mathbb{R})$.

Then for every $\mu > \sigma$,

$$|r_K(t)| \le C_\mu e^{\mu t}, \qquad C_\mu = \frac{1}{2\pi}\int_{-\infty}^{\infty} |R_K(\mu + i\omega)| \, \mathrm{d}\omega. \tag{3.4}$$

Consequently, if α_K denotes the supremum of the real parts of all nondeflated poles and the hypotheses hold for every $\sigma > \alpha_K$, then for every $\varepsilon > 0$,

$$|r_K(t)| \le C_\varepsilon e^{(\alpha_K+\varepsilon)t}. \tag{3.5}$$

Proof. After the selected poles are removed, hypotheses (H1) and (H2) allow the Bromwich contour to be shifted to $\operatorname{Re} s = \mu$ without crossing a residual pole. Thus

$$r_K(t) = \frac{1}{2\pi}\int_{-\infty}^{\infty} e^{(\mu+i\omega)t} R_K(\mu + i\omega) \, \mathrm{d}\omega.$$

Taking absolute values and using (H3) gives equation (3.4). Choosing $\mu = \alpha_K + \varepsilon$ gives equation (3.5). □

The theorem does not say that every additional pair should be removed numerically. It says that exact deflation improves the asymptotic spectral rate. On a fixed mesh, high branches also introduce increasingly oscillatory functions into q_K and hence into the residual history ψ_K. The approximation error therefore reflects a competition between long-time spectral separation and short-time resolvability. This tradeoff is measured in section 6 by a computable residual rather than by branch count alone.

3.2 Exact branch sensitivities

Although not the principal novelty, Lambert branches provide inexpensive parameter derivatives useful for stability tracking.

Proposition 3.1 (Simple-root sensitivities)**.** *For a simple characteristic root,*

$$\begin{aligned}\frac{\partial \lambda_k}{\partial a} &= \frac{1}{1+\tau(\lambda_k - a)},\\ \frac{\partial \lambda_k}{\partial b} &= \frac{\lambda_k - a}{b[1+\tau(\lambda_k - a)]},\\ \frac{\partial \lambda_k}{\partial \tau} &= -\frac{\lambda_k(\lambda_k - a)}{1+\tau(\lambda_k - a)}.\end{aligned}$$

Proof. Implicitly differentiate $\Delta(\lambda_k) = 0$. Since $\Delta_\lambda = 1 + b\tau e^{-\lambda\tau} = 1 + \tau(\lambda - a)$, substitution of $\Delta_a = -1$, $\Delta_b = -e^{-\lambda\tau}$, and $\Delta_\tau = b\lambda e^{-\lambda\tau}$ gives the three identities. □

4 A history-separated least-squares formulation

A key correction to a naive least-squares formulation is that, on the first delay interval, $v(t-\tau)$ is not an unknown value. It is prescribed by the history. Treating the entire delay term as a linear operator on $H^1(0,T)$ is therefore incorrect unless the history contribution is first moved to the right-hand side.

For a residual history ψ define the linear operator

$$(\mathcal{L}_0 v)(t) = v'(t) - av(t) - b\mathbf{1}_{[\tau,T]}(t)v(t-\tau), \qquad v \in H^1(0,T), \tag{4.1}$$

and the data function

$$f_\psi(t) = g(t) + b\mathbf{1}_{(0,\tau)}(t)\psi(t-\tau).$$

Then the residual equation is exactly

$$\mathcal{L}_0 r = f_\psi \quad \text{in } L^2(0,T), \qquad r(0) = \psi(0). \tag{4.2}$$

For $\gamma > 0$, define

$$\mathcal{A}_\gamma v = \big(\mathcal{L}_0 v, \sqrt{\gamma}\, v(0)\big) \in L^2(0,T) \times \mathbb{R},$$

and

$$J_\psi(v) = \|\mathcal{L}_0 v - f_\psi\|^2_{L^2(0,T)} + \gamma\, |v(0) - \psi(0)|^2\,. \tag{4.3}$$

Theorem 4.1 (Finite-horizon stability of the DDE operator)**.** *There exist constants $c_T, C_T > 0$, depending only on T, τ, a, b, and γ, such that*

$$c_T\, \|v\|_{H^1(0,T)} \le \|\mathcal{A}_\gamma v\|_{L^2\times\mathbb{R}} \le C_T\, \|v\|_{H^1(0,T)} \tag{4.4}$$

for every $v \in H^1(0,T)$.

Proof. Set $F = \mathcal{L}_0 v$. From equation (4.1),

$$v(t) = v(0) + \int_0^t \big[av(s) + b\mathbf{1}_{[\tau,T]}(s)v(s-\tau) + F(s)\big]\, \mathrm{d}s.$$

Let $E(t) = \sup_{0\le s\le t} |v(s)|$. Since $|v(s-\tau)| \le E(s)$ whenever $s \ge \tau$,

$$E(t) \le |v(0)| + (|a| + |b|) \int_0^t E(s)\, \mathrm{d}s + \sqrt{T}\, \|F\|_{L^2}\,.$$

Gronwall's inequality gives

$$E(T) \le e^{(|a|+|b|)T}\left(|v(0)| + \sqrt{T}\,\|F\|_{L^2}\right).$$

Hence $\|v\|_{L^2} \le \sqrt{T}E(T)$. Also,

$$\|v'\|_{L^2} \le (|a| + |b|)\,\|v\|_{L^2} + \|F\|_{L^2}.$$

Together these inequalities yield

$$\|v\|_{H^1} \le C\,(|v(0)| + \|\mathcal{L}_0 v\|_{L^2}) \le C'\,\|\mathcal{A}_\gamma v\|_{L^2\times\mathbb{R}},$$

which proves the left inequality. For the upper inequality, the translation $v(\cdot - \tau)$ is bounded from $L^2(0, T-\tau)$ into $L^2(\tau, T)$, and the one-dimensional trace map $H^1(0,T) \to \mathbb{R}$, $v \mapsto v(0)$, is bounded. Thus $\mathcal{A}_\gamma$ is bounded from $H^1(0,T)$ into $L^2(0,T)\times\mathbb{R}$. □

Corollary 4.1 (Least-squares quasi-optimality)**.** *Let $V_h \subset H^1(0,T)$ be a finite-dimensional space, and let r_h minimize J_ψ over V_h. If r is the exact solution of equation* (4.2)*, then*

$$\|r - r_h\|_{H^1(0,T)} \le \frac{C_T}{c_T}\inf_{v_h\in V_h}\|r - v_h\|_{H^1(0,T)}.$$

Proof. Because $\mathcal{A}_\gamma r = (f_\psi, \sqrt{\gamma}\psi(0))$, the minimizer is the orthogonal projection in the $\mathcal{A}_\gamma$ norm. Hence $\|\mathcal{A}_\gamma(r - r_h)\| \le \inf_{v_h\in V_h}\|\mathcal{A}_\gamma(r - v_h)\|$. Apply equation (4.4) to both sides. □

Corollary 4.2 (Residual-based a posteriori bound)**.** *For any trial function $v \in H^1(0,T)$,*

$$\|r - v\|_{H^1(0,T)} \le c_T^{-1}\left(\|\mathcal{L}_0 v - f_\psi\|_{L^2}^2 + \gamma\,|v(0) - \psi(0)|^2\right)^{1/2}.$$

This estimate is the basis for resolution-aware mode selection. It compares candidate deflations using the equation they actually leave for the numerical solver, rather than assuming that a larger number of exact modes must be beneficial.

5 B-spline tight-frame residual discretization

The residual problem in equation (4.2) is approximated in a multilevel piecewise-linear spline space generated from a compactly supported tight-framelet construction. Such frame-based discretizations have proved useful in numerical differential-equation settings because they combine compact support with redundant multiscale representation [13, 15].

5.1 Refinable B-spline and tight-frame generators

Let

$$\varphi(x) = \max(1 - |x|, 0), \qquad x \in \mathbb{R},$$

be the centered linear B-spline. It is compactly supported on $[-1, 1]$, continuous, piecewise linear, and belongs to $H^1(\mathbb{R})$. Its Fourier transform, with the convention $\widehat{f}(\xi) = \int_{\mathbb{R}} f(x)e^{-i\xi x}\,\mathrm{d}x$, is

$$\widehat{\varphi}(\xi) = \left(\frac{\sin(\xi/2)}{\xi/2}\right)^2, \qquad \widehat{\varphi}(0) = 1.$$

The function is refinable and satisfies

$$\varphi(x) = 2\sum_{m=-1}^{1} q_0[m]\varphi(2x - m), \qquad q_0 = \frac{1}{4}[1, 2, 1], \tag{5.1}$$

where the entries of each mask are indexed by $m = -1, 0, 1$.

We use the two high-pass masks

$$q_1 = \frac{\sqrt{2}}{4}[1, 0, -1], \qquad q_2 = \frac{1}{4}[-1, 2, -1], \tag{5.2}$$

and define

$$\psi_\ell(x) = 2 \sum_{m=-1}^{1} q_\ell[m]\varphi(2x - m), \qquad \ell = 1, 2. \tag{5.3}$$

Thus

$$\psi_1(x) = \frac{\sqrt{2}}{2}\big[\varphi(2x + 1) - \varphi(2x - 1)\big],$$
$$\psi_2(x) = -\frac{1}{2}\varphi(2x + 1) + \varphi(2x) - \frac{1}{2}\varphi(2x - 1).$$

Both generators are continuous, piecewise linear, supported on $[-1, 1]$, and belong to $H^1(\mathbb{R})$. The first generator is antisymmetric and has one vanishing moment, whereas the second is symmetric and has two vanishing moments.

To verify the tight-frame condition, introduce the trigonometric symbols

$$\widehat{q}_\ell(\xi) = \sum_{m=-1}^{1} q_\ell[m]e^{-im\xi}, \qquad \ell = 0, 1, 2.$$

For the masks above,

$$\widehat{q}_0(\xi) = \cos^2\left(\frac{\xi}{2}\right), \qquad \widehat{q}_1(\xi) = \frac{i}{\sqrt{2}}\sin\xi, \qquad \widehat{q}_2(\xi) = \sin^2\left(\frac{\xi}{2}\right).$$

A direct calculation gives the two unitary-extension identities

$$\sum_{\ell=0}^{2} |\widehat{q}_\ell(\xi)|^2 = 1, \tag{5.4}$$

$$\sum_{\ell=0}^{2} \widehat{q}_\ell(\xi)\overline{\widehat{q}_\ell(\xi + \pi)} = 0, \qquad \xi \in \mathbb{R}. \tag{5.5}$$

These are precisely the mask relations used by the unitary extension principle for this refinable function [13].

Proposition 5.1 (Full-line Parseval frame)**.** *Let*

$$\psi_{\ell,j,k}(x) = 2^{j/2}\psi_\ell(2^j x - k), \qquad \ell = 1, 2, \quad j, k \in \mathbb{Z}.$$

Then the affine system

$$\mathcal{X}(\Psi) = \{\psi_{\ell,j,k} : \ell = 1, 2,\ j, k \in \mathbb{Z}\}$$

is a Parseval frame for $L^2(\mathbb{R})$. Consequently, for every $f \in L^2(\mathbb{R})$,

$$\|f\|^2_{L^2(\mathbb{R})} = \sum_{\ell=1}^{2} \sum_{j\in\mathbb{Z}} \sum_{k\in\mathbb{Z}} |\langle f, \psi_{\ell,j,k}\rangle|^2, \tag{5.6}$$

$$f = \sum_{\ell=1}^{2} \sum_{j\in\mathbb{Z}} \sum_{k\in\mathbb{Z}} \langle f, \psi_{\ell,j,k}\rangle\, \psi_{\ell,j,k}, \tag{5.7}$$

with convergence of the reconstruction in $L^2(\mathbb{R})$.

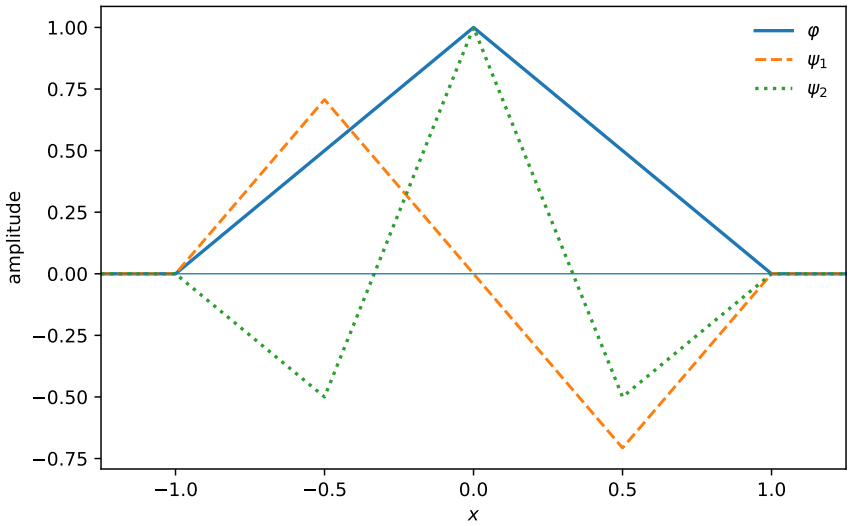


Figure 1: Centered linear B-spline φ and the two compactly supported framelet generators defined by equation (5.3). The antisymmetry of ψ_1 and symmetry of ψ_2 reflect their first- and second-order vanishing-moment structure.

Proof. The centered linear B-spline is compactly supported and refinable, and its low-pass mask is equation (5.1). The identities equations (5.4) and (5.5) verify the unitary extension conditions for the masks q_0, q_1, q_2. The conclusion follows from the unitary extension principle [13]. □

The vanishing moments can also be read directly from the mask symbols. Since $\widehat{\psi}_\ell(\xi) = \widehat{q}_\ell(\xi/2)\widehat{\varphi}(\xi/2)$, the simple zero of $\widehat{q}_1$ at the origin gives $\int_{\mathbb{R}} \psi_1(x)\,\mathrm{d}x = 0$, while the double zero of $\widehat{q}_2$ gives

$$\int_{\mathbb{R}} \psi_2(x)\,\mathrm{d}x = 0, \qquad \int_{\mathbb{R}} x\psi_2(x)\,\mathrm{d}x = 0.$$

The two generators therefore play complementary roles: ψ_1 detects first-order variation, whereas ψ_2 annihilates affine data and is more selective for curvature-type detail.

Figure 1 displays the centered B-spline and the two framelet generators used in the discretization.

The corresponding frequency-domain energy partition is shown in Figure 2, providing a direct visual check of the UEP filter identity.

5.2 Multilevel spline space and restriction to the time interval

For $j, k \in \mathbb{Z}$, define

$$\varphi_{j,k}(x) = 2^{j/2}\varphi(2^j x - k), \qquad V_j = \overline{\operatorname{span}\{\varphi_{j,k} : k \in \mathbb{Z}\}}^{L^2(\mathbb{R})}.$$

The spaces are nested, $V_j \subset V_{j+1}$, and V_j consists of continuous piecewise-linear splines with knots on the grid $2^{-j}\mathbb{Z}$. The refinement relation and the UEP filter bank imply the multilevel decomposition

$$V_J = V_{J_0} + \sum_{j=J_0}^{J-1} \operatorname{span}\{\psi_{\ell,j,k} : \ell = 1, 2,\ k \in \mathbb{Z}\}, \qquad J > J_0,$$

where the sum is not direct because the framelet representation is redundant.

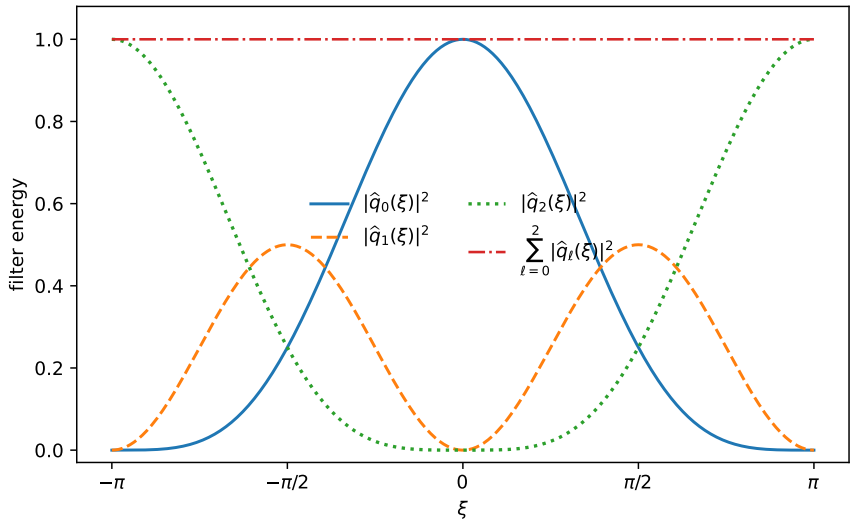


Figure 2: Frequency-domain partition associated with the masks equations (5.1) and (5.2). The sum $\sum_{\ell=0}^{2} |\widehat{q}_\ell(\xi)|^2$ is identically one; the numerical plotting residual is below 5×10^{-16}. This identity, together with the alias-cancellation relation equation (5.5), verifies the tight-frame filter conditions.

The numerical problem is posed in physical time $t \in [0, T]$. With $x = t/T$, the atoms used in the code are

$$\varphi_{j,k}^{T}(t) = 2^{j/2} \varphi\left(2^j \frac{t}{T} - k\right),$$
$$\psi_{\ell,j,k}^{T}(t) = 2^{j/2} \psi_\ell\left(2^j \frac{t}{T} - k\right).$$

A common factor $T^{-1/2}$ would make this change of variables unitary in L^2, but it is omitted in the implementation because multiplying every dictionary column by the same nonzero constant changes only the coefficient scaling, not the trial space or the reconstructed least-squares trajectory. The derivative used in the DDE operator is obtained by the chain rule, for example

$$\frac{\mathrm{d}}{\mathrm{d}t} \psi_{\ell,j,k}^{T}(t) = \frac{2^{3j/2}}{T} \psi_\ell'\left(2^j \frac{t}{T} - k\right) \quad \text{a.e. on } (0, T).$$

Because $\operatorname{supp} \varphi = \operatorname{supp} \psi_\ell = [-1, 1]$, only shifts $k = 0, \ldots, 2^j$ have support of positive measure in $[0, 1]$ after restriction. We therefore use

$$\mathcal{D}_{J_0,J} = \{\varphi_{J_0,k}^{T} : 0 \le k \le 2^{J_0}\} \cup \{\psi_{\ell,j,k}^{T} : \ell = 1, 2,\ J_0 \le j < J,\ 0 \le k \le 2^j\}. \tag{5.8}$$

The corresponding number of synthesis columns is

$$N_{\mathrm{col}} = (2^{J_0} + 1) + 2 \sum_{j=J_0}^{J-1} (2^j + 1).$$

Let V_J^T denote the continuous piecewise-linear spline space on the physical mesh

$$0 = t_0 < t_1 < \cdots < t_{2^J} = T, \qquad t_m = \frac{mT}{2^J}.$$

The restricted dictionary equation (5.8) spans V_J^T. In particular,

$$\dim V_J^T = 2^J + 1, \qquad \operatorname{rank} \mathcal{D}_{J_0,J} = 2^J + 1,$$

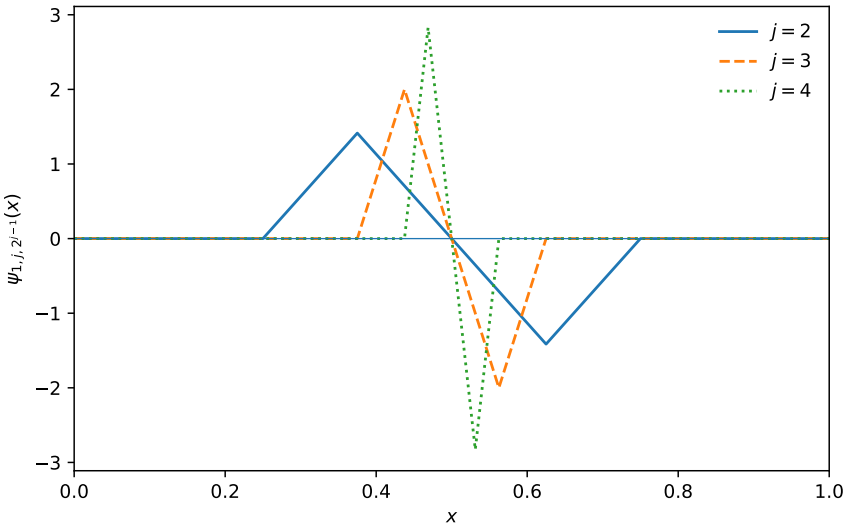


Figure 3: Dyadic localization of the first framelet generator. The functions $\psi_{1,j,2^{j-1}}$ are centered at $x = 1/2$; increasing j contracts their support while preserving the usual $2^{j/2}$ amplitude normalization.

while $N_{\mathrm{col}} > 2^J + 1$ for $J > J_0$. Thus the finite system used in the computation is a redundant spanning family, not a basis.

Remark 5.1 (Boundary restriction and tightness). The Parseval identities equations (5.6) and (5.7) belong to the full-line affine system. Restricting its elements to a bounded interval and truncating the scale range changes the frame operator near the boundary. We therefore refer to equation (5.8) as a *tight-frame dictionary*: its atoms are generated by a full-line Parseval frame, but the finite interval dictionary is not assumed to satisfy an exact Parseval identity. No orthogonality or linear independence is used in the numerical analysis.

The dyadic localization of the first generator across three refinement levels is illustrated in Figure 3.

The use of the linear B-spline is particularly convenient for the present DDE residual. The trial functions lie in $H^1(0,T)$, as required by theorem 4.1; their supports are local; delay translation simply shifts the same piecewise-linear atoms; and refinement of J produces the standard linear-spline approximation order without changing the analytical least-squares formulation.

5.3 From the frame dictionary to the least-squares system

Enumerate the functions in equation (5.8) as $\{\chi_n\}_{n=1}^{N_{\mathrm{col}}}$ and write the numerical residual as

$$r_h(t) = \sum_{n=1}^{N_{\mathrm{col}}} c_n \chi_n(t).$$

This is a synthesis expansion. The coefficients c_n are *not* the canonical full-line frame coefficients $\langle r, \psi_{\ell,j,k}\rangle$ from equation (5.7). They are determined by the DDE least-squares problem after interval restriction and therefore depend on the operator $\mathcal{L}_0$, the history, and the initial-condition penalty.

Let $\{t_i, w_i\}_{i=1}^{N_q}$ be the three-point Gauss–Legendre nodes and weights applied cell by cell on the finest dyadic mesh. Define

$$A_{in} = \sqrt{w_i}\left[\chi_n'(t_i) - a\chi_n(t_i) - b\mathbf{1}_{[\tau,T]}(t_i)\chi_n(t_i-\tau)\right], \tag{5.9}$$

and

$$F_i = \sqrt{w_i}\left[g(t_i) + b\mathbf{1}_{(0,\tau)}(t_i)\psi(t_i - \tau)\right]. \tag{5.10}$$

The initial condition contributes the weighted row

$$A_{0n} = \sqrt{\gamma}\,\chi_n(0), \qquad F_0 = \sqrt{\gamma}\,\psi(0). \tag{5.11}$$

Thus the discrete counterpart of J_ψ in equation (4.3) is

$$\boldsymbol{c} = \operatorname*{argmin}_{\boldsymbol{z}\in\mathbb{R}^{N_{\mathrm{col}}}} \|A\boldsymbol{z} - F\|_2 . \tag{5.12}$$

For the delay-aligned meshes used in the experiments, χ_n', χ_n, and the shifted term $\chi_n(\,\cdot - \tau)$ are piecewise polynomial on each quadrature cell. Three-point Gauss–Legendre quadrature therefore resolves the polynomial part of the operator products exactly; only the nonpolynomial data g and the prescribed history are subject to quadrature error.

Because the synthesis dictionary is redundant, equation (5.12) can have many coefficient vectors representing the same trial function. We use the minimum-Euclidean-norm solution obtained from a truncated singular-value decomposition. If

$$A = U\Sigma V^*, \qquad \sigma_1 \geq \cdots \geq \sigma_s \geq 0,$$

and

$$r_A = \max\{m : \sigma_m \geq 10^{-11}\sigma_1\},$$

then

$$\boldsymbol{c} = V_{r_A}\Sigma_{r_A}^{-1}U_{r_A}^* F.$$

The threshold is relative, so a uniform rescaling of all frame columns does not change the retained numerical rank. The penalty is $\gamma = 10^6$ in all reported experiments.

5.4 Approximation estimate

The frame representation does not alter the underlying approximation class: the trial space is the continuous linear-spline space V_J^T. Consequently, the standard spline estimate can be combined directly with the least-squares quasi-optimality result corollary 4.1.

Proposition 5.2 (First-order H^1 approximation)**.** *Let $h = T2^{-J}$, let the dyadic mesh contain all delay-propagation points in $[0,T]$, and let $r_h \in V_J^T$ be the least-squares approximation of the exact residual r. If $r \in H^2_{\mathrm{pw}}(0,T)$ with respect to the delay-induced subinterval partition, then*

$$\|r - r_h\|_{H^1(0,T)} \leq Ch\,\|r\|_{H^2_{\mathrm{pw}}(0,T)}, \tag{5.13}$$

where C is independent of h.

Proof. Let $I_h r \in V_J^T$ be the nodal piecewise-linear interpolant on the delay-aligned mesh. On each subinterval on which $r \in H^2$, the standard linear-spline estimate gives

$$\|r - I_h r\|_{H^1} \leq C_I h\,\|r\|_{H^2_{\mathrm{pw}}}.$$

Since equation (5.8) spans V_J^T, the interpolant is representable by the frame dictionary. Applying corollary 4.1 with $v_h = I_h r$ yields

$$\|r - r_h\|_{H^1} \leq \frac{C_T}{c_T} C_I h\,\|r\|_{H^2_{\mathrm{pw}}},$$

which proves equation (5.13). □

Remark 5.2 (What the estimate does and does not imply). Proposition 5.2 gives first-order convergence in the H^1 norm. The approximately second-order maximum and RMS rates observed for the smooth manufactured solution in section 7.1 are empirical trajectory rates and are not claimed as a consequence of the H^1 estimate.

6 Resolution-aware deflation algorithm and long-time windowing

The deflated approximation is

$$u_{h,K}(t) = q_K(t) + r_{h,K}(t).$$

Since q_K is exact, the total numerical error is exactly the residual approximation error,

$$u - u_{h,K} = r_K - r_{h,K}.$$

This identity makes the residual estimator in corollary 4.2 directly relevant to mode selection.

For a candidate sequence of conjugate-pair sets $K_0 \subset K_1 \subset \cdots \subset K_P$, define the computable discrete indicator

$$\widehat{\eta}_p = \left(\sum_i w_i \left| (\mathcal{L}_0 r_{h,K_p})(t_i) - f_{\psi_{K_p}}(t_i) \right|^2 + \gamma \left| r_{h,K_p}(0) - \psi_{K_p}(0) \right|^2 \right)^{1/2}. \tag{6.1}$$

It is a quadrature approximation to the rigorous residual norm in corollary 4.2. The proposed resolution-aware rule is

$$p_h = \operatorname*{argmin}_{0 \le p \le P} \widehat{\eta}_p. \tag{6.2}$$

All candidates share the same matrix A because the operator and numerical space are unchanged; only the right-hand side changes. Thus one matrix factorization can be reused for several candidate deflations. This is computationally preferable to selecting p solely from spectral location.

The spectral-gap result motivates an additional long-time device. Let $T_w < T$ be a transient window. Compute the residual numerically only on $[0, T_w]$, and for $t > T_w$ use

$$u_{\mathrm{win}}(t) = q_K(t).$$

If the first nondeflated spectral abscissa is sufficiently negative, theorem 3.2 controls the discarded tail. In practice T_w is chosen so that either an analytical tail estimate or an independently computed high-accuracy residual falls below the desired tolerance. The experiment in section 7.3 quantifies this idea.

7 Numerical experiments

The numerical experiments were implemented using high-precision arithmetic for the Lambert-W branches together with standard scientific linear-algebra and high-order time-integration routines. The complete computational procedure follows algorithm 1. The common numerical settings are summarized in table 1; experiment-specific modifications are stated explicitly where they occur.

Unless an exact solution is available, an independent reference trajectory is computed by the method of steps. On each interval of length τ, the resulting ordinary differential equation is solved with a high-order adaptive integrator using stringent local error tolerances and a maximum step size not exceeding $\tau/200$. This interval-by-interval continuous-ODE construction is consistent with the standard method-of-steps treatment of retarded delay differential equations [2, 3].

7.1 Experiment 1: smooth manufactured solution

We first test the residual discretization without relying on a Lambert representation. Set

$$a = -0.7, \qquad b = 0.6, \qquad \tau = 0.5, \qquad T = 4,$$

Algorithm 1 Lambert-W spectral deflation with tight-frame least squares and residual-based mode selection

Require: a, b, τ, T, history ϕ, forcing g, frame levels J_0, J, maximum candidate pair count P.

1: Compute candidate Lambert roots λ_k and, for the homogeneous core, residues c_k from equation (2.5).
2: Assemble the history-separated least-squares matrix A once using equations (5.9) and (5.11).
3: Compute a rank-revealing factorization of A.
4: **for** $p = 0, 1, \ldots, P$ **do**
5: Form q_{K_p} and residual history $\psi_{K_p} = \phi - q_{K_p}$.
6: Assemble only the right-hand side F_p from equations (5.10) and (5.11).
7: Solve the least-squares problem using the stored factorization.
8: Evaluate $\widehat{\eta}_p$ from equation (6.1).
9: **end for**
10: Select p_h by equation (6.2) and return $u_{h,K_{p_h}} = q_{K_{p_h}} + r_{h,K_{p_h}}$.
11: **if** long-time windowing is requested **then**
12: Choose T_w after the residual tail is below tolerance, solve r_h only on $[0, T_w]$, and use q_K for $t > T_w$.
13: **end if**

and prescribe, on both the history and solution interval,

$$u_{\mathrm{ex}}(t) = e^{-0.4t}\big(1 + 0.2\sin(3t)\big).$$

The forcing is manufactured exactly as

$$g(t) = u'_{\mathrm{ex}}(t) - a u_{\mathrm{ex}}(t) - b u_{\mathrm{ex}}(t-\tau).$$

Because $\tau/T = 1/8$, every delay junction is aligned with the dyadic meshes used below.

Table 2 and Figure 4 show essentially second-order decay in both maximum and RMS errors. This is stronger than the H^1 estimate proved in proposition 5.2, but it is consistent with the smoothness of the exact solution and the piecewise-linear approximation in the reported trajectory norms.

7.2 Experiment 2: weakly damped oscillation and exact pole removal

Consider

$$u'(t) = -u(t) - 2u(t-1), \qquad \phi(t) \equiv 1, \quad -1 \le t \le 0. \tag{7.1}$$

The rightmost Lambert pair is

$$\lambda_{0,-1} = -0.0924843222914664 \;\pm\; 1.997282691039464\, i,$$

and using the constant-history expression equation (2.6), the corresponding residues are

$$c_{0,-1} = 0.409815139968218 \pm 0.356647314630680\, i.$$

The next pair has real part -1.363019832881977 and frequency 7.807518913600586. Thus, exact cancellation of the dominant pair creates a large asymptotic spectral gap, but cancellation of the next pair also injects a substantially higher frequency into the residual history.

Before using the frame discretization, table 3 validates the residue formula directly against the method-of-steps reference. The error is measured only after one or two delay intervals because finite modal sums are not expected to reproduce arbitrary history compatibility at $t = 0$ uniformly.

Table 1: Numerical and reproducibility settings used throughout the computational experiments.

Quantity	**Value**
Lambert-W arithmetic	50-digit working precision
Frame coarse level	$J_0 = 2$
Reported finest levels	$J = 5, 6, 7, 8$
Quadrature	3-point Gauss–Legendre per finest cell
Initial-condition penalty	$\gamma = 10^6$
Least-squares rank threshold	10^{-11} relative singular value
Reference procedure	Method of steps with high-order adaptive integration
Default relative tolerance	2×10^{-12}
Default absolute tolerance	2×10^{-14}
Reference maximum step	$\leq \tau/200$
Long-time reference tolerances	$(3 \times 10^{-12}, 3 \times 10^{-14})$
Weakly damped benchmark	$a = -1$, $b = -2$, $\tau = 1$, $\phi \equiv 1$
Frame-comparison horizon	$T = 8$
Long-time horizon and residual window	$T = 50$, $T_w = 8$
Manufactured-solution test	$a = -0.7$, $b = 0.6$, $\tau = 0.5$, $T = 4$

Table 2: Manufactured-solution convergence of the B-spline framelet least-squares method.

J	h	columns	rank	$\|e\|_\infty$	rate	RMS error
5	0.125000	67	33	2.421×10^{-3}	–	7.914×10^{-4}
6	0.062500	133	65	6.126×10^{-4}	1.982	1.977×10^{-4}
7	0.031250	263	129	1.535×10^{-4}	1.997	4.943×10^{-5}
8	0.015625	521	257	3.838×10^{-5}	2.000	1.236×10^{-5}

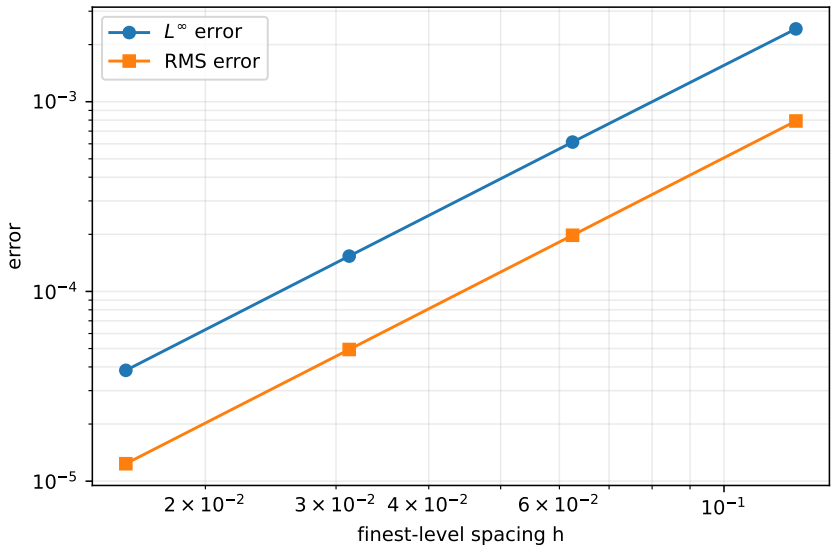


Figure 4: Manufactured-solution convergence. Both maximum and RMS trajectory errors decrease at approximately second order under dyadic refinement.

The more relevant test compares the same frame discretization with zero, one, two, or three conjugate pairs removed. All candidates use the same trial dictionary, quadrature rule, SVD rank threshold, mesh, and least-squares matrix; only the residual history and right-hand side change.

Table 3: Pure Lambert modal truncation for equation (7.1).

conjugate pairs	$\max_{t\geq 1} \lvert u-q\rvert$	$\max_{t\geq 2} \lvert u-q\rvert$
1	2.020×10^{-2}	7.033×10^{-3}
2	4.580×10^{-3}	8.134×10^{-4}
3	1.983×10^{-3}	2.271×10^{-4}
5	7.081×10^{-4}	4.617×10^{-5}
10	1.784×10^{-4}	5.467×10^{-6}
20	4.509×10^{-5}	6.629×10^{-7}
40	1.128×10^{-5}	8.158×10^{-8}

Table 4: Maximum error for direct and deflated frame solves on $[0, 8]$. The matrix is identical across each row block; only the right-hand side changes.

J	h	no deflation	1 pair	2 pairs	3 pairs
5	0.25000	1.335×10^{-1}	3.838×10^{-2}	5.202×10^{-2}	4.872×10^{-2}
6	0.12500	3.786×10^{-2}	1.076×10^{-2}	1.865×10^{-2}	2.404×10^{-2}
7	0.06250	9.779×10^{-3}	2.816×10^{-3}	5.299×10^{-3}	7.596×10^{-3}
8	0.03125	2.463×10^{-3}	7.186×10^{-4}	1.392×10^{-3}	2.061×10^{-3}

We use $T = 8$, so the dyadic mesh is aligned with the unit delay. The results are in table 4. At every tested level the one-pair scheme is the most accurate in maximum norm. At $J = 8$, the maximum error falls from 2.463×10^{-3} without deflation to 7.186×10^{-4} with one pair, a factor of 3.43. The RMS error improves by a factor of 9.67. Because the effective rank remains 257 in both cases, this is a fixed-resolution and fixed-rank comparison rather than an accuracy gain obtained by enlarging the discrete space. Two or three pairs are worse at the same mesh because their more oscillatory residual histories are under-resolved relative to the dominant-pair residual.

Table 5 isolates the numerical effect of spectral deflation at fixed discrete complexity. The improvement occurs without changing the matrix dimension, numerical rank, or matrix condition number, supporting the interpretation that deflation improves the approximability of the residual rather than preconditioning the linear algebra.

The refinement trends for the undeflated and deflated formulations are compared in Figure 5.

At the finest reported level, Figure 6 shows how the error changes as additional conjugate pairs are removed.

The discrete residual indicator at $J = 8$ is 5.729×10^{-2}, 2.757×10^{-2}, 3.449×10^{-2}, and 4.186×10^{-2} for zero, one, two, and three pairs, respectively. It therefore selects the same one-pair model as the true error, without access to the reference solution. This agreement is precisely the use intended for equation (6.2).

An important negative result is equally useful. For $J = 8$, the nonzero singular-value condition number of the least-squares matrix is 8.72×10^3 for all four deflation choices. This is expected because the matrix A in equation (5.9) is unchanged. Deflation is therefore not a linear-algebra preconditioner. Its numerical advantage comes from changing the residual data, not from making the same matrix better conditioned.

The corresponding reference, direct, and one-pair deflated trajectories are shown in Figure 7.

7.3 Experiment 3: long-time windowing

The same weakly damped problem is integrated to $T = 50$. After the dominant pair is removed, the next pair has real part -1.3630, so the remaining free response should decay much faster than the original envelope, whose dominant real part is only -0.09248. The measured tail errors

Table 5: Controlled fixed-rank comparison at $J = 8$. Both formulations use the same 521 synthesis columns, effective rank 257, quadrature, SVD threshold, and least-squares matrix.

Formulation	Effective rank	$\|e\|_\infty$	RMS error	$\kappa_2(A)$
Direct tight-frame least squares	257	2.463×10^{-3}	1.401×10^{-3}	8.72×10^{3}
One-pair deflated least squares	257	7.186×10^{-4}	1.450×10^{-4}	8.72×10^{3}

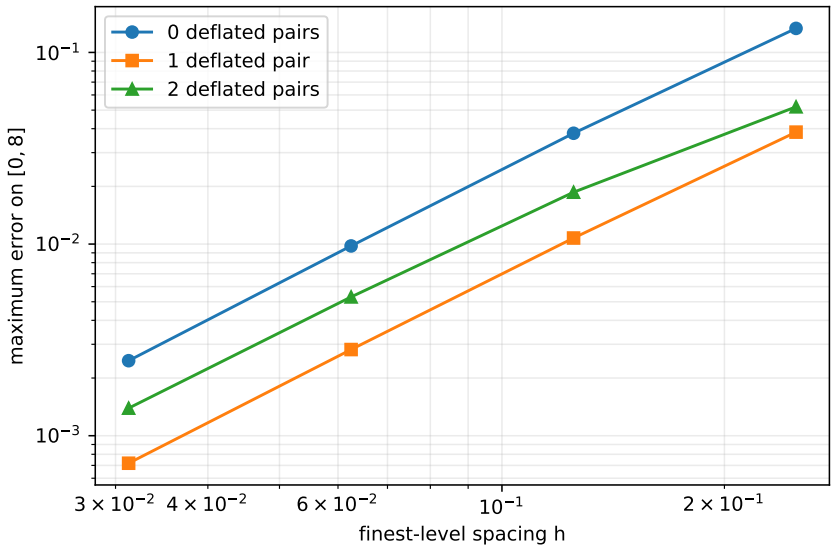


Figure 5: Maximum error under mesh refinement for the undeflated method and for one or two deflated conjugate pairs. The dominant-pair residual is consistently easiest to resolve.

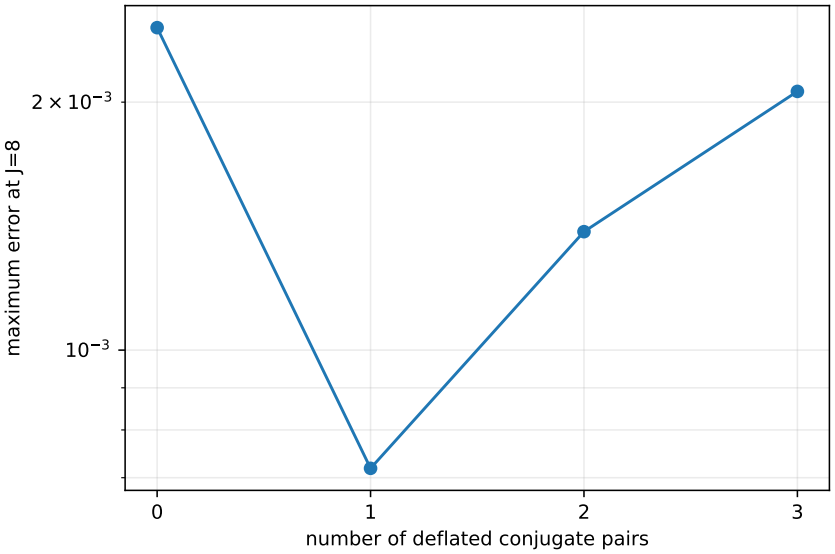


Figure 6: Resolution-aware mode selection at $J = 8$. More exact modes do not automatically improve the fixed-resolution computation.

in table 6 confirm this separation.

The accelerated decay of the residual after dominant-pair removal is shown in Figure 8.

We therefore solve the frame residual only on $[0, 8]$ with $J = 8$ and spacing $h = 1/32$. For

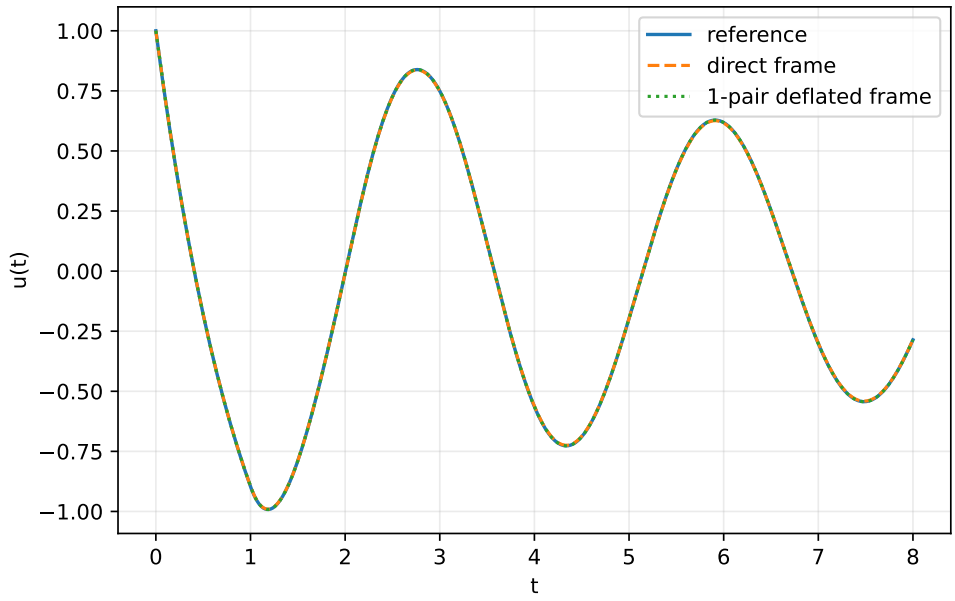


Figure 7: Reference, direct frame, and dominant-pair deflated frame solutions for equation (7.1) at $J = 8$. The curves are visually close; the error tables quantify the difference.

Table 6: Maximum dominant-pair residual after selected times for equation (7.1).

t_0	$\max_{t \geq t_0} \lvert u(t) - q_1(t) \rvert$
2	7.033×10^{-3}
4	4.140×10^{-4}
6	2.606×10^{-5}
8	1.668×10^{-6}
10	1.073×10^{-7}
12	6.906×10^{-9}
15	9.051×10^{-11}
20	1.077×10^{-13}

$t > 8$, only the dominant analytic pair is retained. On the full interval $[0, 50]$, this windowed approximation has maximum error 7.182×10^{-4}. The q-only tail beyond 8 contributes at most 1.668×10^{-6}, so the global error is controlled by the finite-window frame error rather than by the long-time truncation. At the same local spacing, a direct piecewise-linear representation over all of $[0, 50]$ would require approximately 1601 effective nodal degrees of freedom, compared with rank 257 for the residual window plus two analytic modes, a representation reduction of about 6.23.

This comparison is a degree-of-freedom count, not a CPU benchmark. A full-horizon adaptive DDE solver does not store one global spline coefficient per cell in the same manner, so no claim of a sixfold runtime speedup is made.

Figure 9 reports the absolute error of the hybrid approximation and identifies the transition at the residual window endpoint $T_w = 8$.

7.4 Experiment 4: delay-induced Hopf crossing

Consider

$$u'(t) = -\alpha u(t) - \beta u(t - \tau), \qquad \alpha = 1, \quad \beta = 2. \tag{7.2}$$

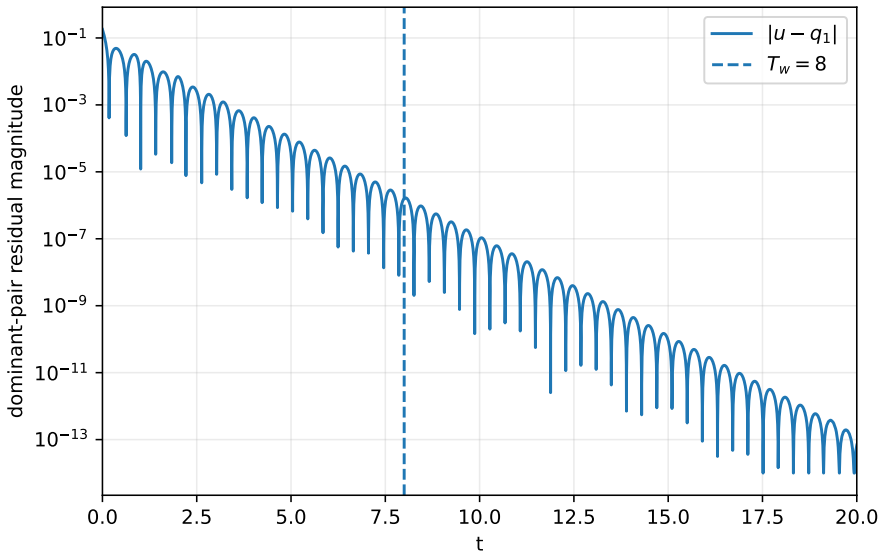


Figure 8: Magnitude of the residual after the dominant Lambert pair has been removed. The rapid post-transient decay makes a finite residual window effective.

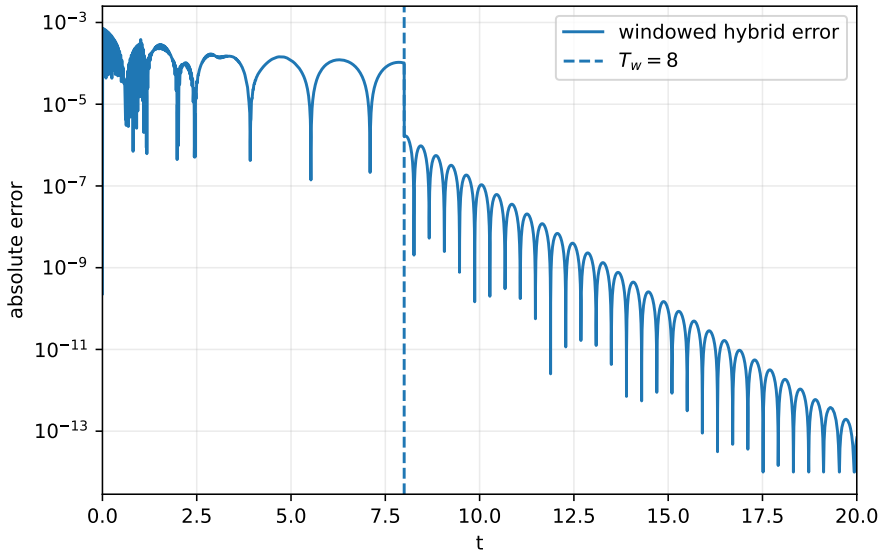


Figure 9: Absolute error of the hybrid windowed approximation on $[0, 20]$. At $T_w = 8$ the numerical residual is switched off and the analytic dominant pair is continued alone.

At a purely imaginary characteristic root $\lambda = i\omega$,

$$i\omega + 1 + 2e^{-i\omega\tau} = 0.$$

Separating real and imaginary parts gives $1 + 2\cos(\omega\tau) = 0$ and $\omega - 2\sin(\omega\tau) = 0$. The first crossing with positive frequency is

$$\omega_c = \sqrt{3}, \qquad \tau_c = \frac{2\pi}{3\sqrt{3}} = 1.209199576156145\ldots.$$

The Lambert roots recover the same crossing. Selected values are shown in Table 7, and Figure 10 shows the rightmost real part changing sign at τ_c.

Table 7: Dominant root of equation (7.2) from Lambert branches.

τ	$\operatorname{Re}\lambda_*$	$\lvert\operatorname{Im}\lambda_*\rvert$
0.50	−0.9310186622	3.1849035750
1.00	−0.0924843223	1.9972826910
1.15	−0.0208216089	1.7992858118
1.2091995762	≈ 0	1.7320508076
1.25	0.0125006351	1.6887182258
1.30	0.0260608501	1.6386411182
1.50	0.0656177111	1.4661868521

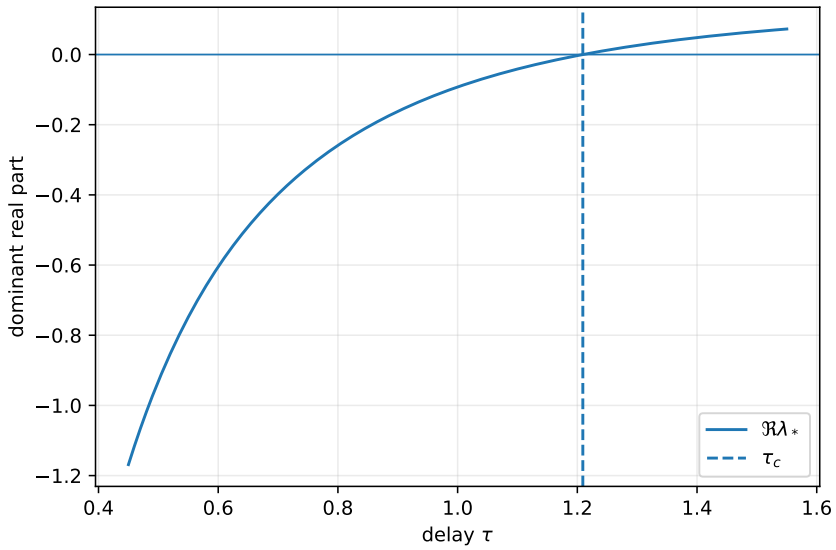


Figure 10: Real part of the dominant characteristic root for equation (7.2). The zero crossing agrees with the analytical value $\tau_c = 2\pi/(3\sqrt{3})$.

The test is not presented as a new Hopf theorem. Its purpose is validation: the same branch computation used for deflation also reproduces a known stability boundary, and proposition 3.1 supplies its local parameter sensitivity without finite differences.

8 Comparison with existing numerical approaches

The proposed method occupies a different position from general-purpose DDE time stepping. Continuous Runge-Kutta and method-of-steps solvers are more general and are preferable when only a trajectory over a moderate horizon is required [2, 3]. They also handle changing histories naturally. The present method becomes attractive when the same spectral modes govern long transients, when many parameter values are examined, or when one wants a compact global representation in which the slow modes are explicit.

Global spectral collocation can converge geometrically for smooth functional differential equations, particularly when the interval is partitioned at propagated discontinuities [12]. Pseudospectral schemes also provide strong tools for approximating characteristic roots and stability [10, 11]. In contrast, the frame residual uses only piecewise-linear local functions in the present implementation, so it should not be expected to beat a well-resolved Chebyshev method on a globally analytic solution. Its advantages are compact support, transparent local refinement, and compatibility with histories that are only piecewise smooth.

Recent wavelet DDE methods demonstrate the usefulness of localized approximation but generally discretize the full solution directly [14, 16–19]. The present contribution is orthogonal to the choice of wavelet family: exact rightmost modes are removed before the local discretization. The direct-versus-deflated comparison in table 4 isolates that contribution because both sides use exactly the same frame dictionary, quadrature, matrix, and solver.

The method also has clear limitations. It requires a reliable spectral representation of the modes to be removed. In the scalar one-delay case this is exact. For systems, matrix Lambert formulas can have nontrivial branch-to-root structure [7–9]; in such cases the deflation idea could still be used, but the roots and eigenvectors should be computed by an independent validated spectral method rather than by assuming a scalar-like branch correspondence. Multiple delays likewise require a different spectral engine. Neutral equations may involve generalized Lambert functions and stronger regularity issues [20].

9 Discussion

The computations support four conclusions that are more informative than a simple claim of improved accuracy. First, exact dominant-mode removal can materially reduce the error of a fixed local approximation. In the principal benchmark the improvement is visible in both maximum and RMS norms across all tested levels. Second, the benefit is not monotone in the number of removed modes. The second and third conjugate pairs have increasingly large imaginary parts, so at fixed h they make the residual history more oscillatory even though the asymptotic spectral gap becomes larger. The minimum of the discrete residual correctly identifies the dominant-pair choice in the tested case.

Third, deflation leaves the least-squares matrix unchanged. This observation prevents a potentially misleading interpretation of the method as a condition-number preconditioner. The measured nonzero singular-value condition number is identical for zero through three deflated pairs. The gain arises because the same finite-dimensional operator is asked to approximate a different, easier residual.

Fourth, the strongest structural advantage appears on long intervals. Once the dominant pair is exact and the residual has decayed at the rate associated with the next spectral pair, the numerical component can be stopped. For equation (7.1), the dominant-pair residual is already below 1.7×10^{-6} after eight delay intervals. The hybrid approximation then carries the weakly damped oscillation analytically to $T = 50$ without extending the frame grid over the entire horizon.

The present theory is finite-horizon in its least-squares part and asymptotic in its spectral part. The two estimates deliberately remain separate. The coercivity theorem controls the numerical residual on $[0, T_w]$, while the spectral-gap theorem controls the analytic tail under its contour assumptions. A sharper combined estimate with computable constants would be valuable, but claiming one from the present ingredients would go beyond what has been proved.

10 Conclusions

A numerical algorithm has been developed for scalar constant-delay retarded equations by combining exact Lambert-W pole cancellation with a localized B-spline framelet least-squares discretization. The main analytical steps are exact finite deflation, a conditional spectral-gap decay theorem, a corrected history-separated least-squares operator, finite-horizon H^1 stability, quasi-optimality, and a residual-based error estimate. The implementation retains the redundancy of the framelet dictionary, solves the resulting rank-deficient system with a rank-revealing least-squares factorization, and reuses that factorization across candidate deflations because the discrete operator is unchanged.

The experiments clarify when the algorithm provides a numerical advantage. A smooth manufactured problem gives essentially second-order trajectory errors. For the weakly damped benchmark, dominant-pair deflation reduces the maximum error by a factor of 3.43 and the RMS error by a factor of 9.67 at the same effective rank 257, while removing additional high-frequency pairs at the same resolution is counterproductive. The least-squares residual detects this behavior and supplies a practical mode-selection criterion. On a long horizon, the spectral gap after dominant-pair removal permits the frame residual to be restricted to a short transient window, after which the analytic mode alone reproduces the solution to a much smaller tail tolerance.

The principal limitation is the exact spectral engine: the simple Lambert branch formula is specific to the scalar single-delay problem. A credible extension to systems should combine the same deflation logic with a validated characteristic-root computation and should not assume a one-to-one matrix-Lambert branch correspondence. Further work should also investigate adaptive local refinement of the residual, higher-order compactly supported framelets, and a posteriori selection of the window length with fully computable constants.

Reproducibility and data availability

No external data set is used.

Funding

This research was supported by the Research Incentive Fund (RIF), Grant No. 23210.

Conflict of interest

The author declares no conflict of interest.

Author contributions

Mutaz Mohammad: conceptualization, methodology, mathematical analysis, software design, validation, visualization, writing, and revision.

References

[1] J. K. Hale and S. M. Verduyn Lunel, *Introduction to Functional Differential Equations*. Springer, New York, 1993. doi:10.1007/978-1-4612-4342-7.

[2] A. Bellen and M. Zennaro, *Numerical Methods for Delay Differential Equations*. Oxford University Press, Oxford, 2003. doi:10.1093/acprof:oso/9780198506546.001.0001.

[3] L. F. Shampine and S. Thompson, "Solving DDEs in Matlab," *Applied Numerical Mathematics*, vol. 37, no. 4, pp. 441-458, 2001. doi:10.1016/S0168-9274(00)00055-6.

[4] R. M. Corless, G. H. Gonnet, D. E. G. Hare, D. J. Jeffrey, and D. E. Knuth, "On the Lambert W function," *Advances in Computational Mathematics*, vol. 5, pp. 329-359, 1996. doi:10.1007/BF02124750.

[5] F. M. Asl and A. G. Ulsoy, "Analysis of a system of linear delay differential equations," *Journal of Dynamic Systems, Measurement, and Control*, vol. 125, no. 2, pp. 215-223, 2003. doi:10.1115/1.1568121.

[6] S. Yi, P. W. Nelson, and A. G. Ulsoy, *Time-Delay Systems: Analysis and Control Using the Lambert W Function*. World Scientific, Singapore, 2010. doi:10.1142/7759.

[7] C. Hwang and Y.-C. Cheng, "A note on the use of the Lambert W function in the stability analysis of time-delay systems," *Automatica*, vol. 41, no. 11, pp. 1979-1985, 2005. doi:10.1016/j.automatica.2005.05.020.

[8] E. Jarlebring and T. Damm, "The Lambert W function and the spectrum of some multidimensional time-delay systems," *Automatica*, vol. 43, no. 12, pp. 2124-2128, 2007. doi:10.1016/j.automatica.2007.04.001.

[9] R. Cepeda-Gomez and W. Michiels, "Some special cases in the stability analysis of multidimensional time-delay systems using the matrix Lambert W function," *Automatica*, vol. 53, pp. 339-345, 2015. doi:10.1016/j.automatica.2015.01.016.

[10] D. Breda, S. Maset, and R. Vermiglio, "Pseudospectral approximation of eigenvalues of derivative operators with non-local boundary conditions," *Applied Numerical Mathematics*, vol. 56, no. 3-4, pp. 318-331, 2006. doi:10.1016/j.apnum.2005.04.011.

[11] F. Scarabel and R. Vermiglio, "Equations with infinite delay: pseudospectral discretization for numerical stability and bifurcation in an abstract framework," *SIAM Journal on Numerical Analysis*, vol. 62, no. 4, pp. 1736-1758, 2024. doi:10.1137/23M1581133.

[12] N. Hale, "A spectral collocation method for functional and delay differential equations," *IMA Journal of Numerical Analysis*, vol. 45, no. 5, pp. 2921-2947, 2025. doi:10.1093/imanum/drae079.

[13] I. Daubechies, B. Han, A. Ron, and Z. Shen, "Framelets: MRA-based constructions of wavelet frames," *Applied and Computational Harmonic Analysis*, vol. 14, no. 1, pp. 1-46, 2003. doi:10.1016/S1063-5203(02)00511-0.

[14] M. Mohammad and A. Trounev, "A new technique for solving neutral delay differential equations based on Euler wavelets," *Complexity*, vol. 2022, art. 1753992, pp. 1-8, 2022. doi:10.1155/2022/1753992.

[15] M. Mohammad, "A tight wavelet frames-based method for numerically solving fractional Riccati differential equations," *Mathematical Methods in the Applied Sciences*, first published 2 March 2025. doi:10.1002/mma.10784.

[16] H. Mohammadi, H. Saeedi, and M. Izadi, "A novel design of Krawtchouk wavelet based projection approach to solve the nonlinear fractional delay differential equations," *Journal of Nonlinear Mathematical Physics*, vol. 32, art. 1, 2025. doi:10.1007/s44198-024-00256-3.

[17] R. Aggarwal, G. Methi, and R. P. Agarwal, "Stability and numerical solutions of higher-order nonlinear time-dependent delay differential equations using Haar wavelet collocation method," *Boundary Value Problems*, vol. 2025, art. 169, 2025. doi:10.1186/s13661-025-02150-3.

[18] N. Khan, M. Asif, M. Ahsan, N. Ullah, and I.-L. Popa, "A robust high-order Haar wavelet collocation method for linear and nonlinear delay differential equations: theoretical analysis and numerical validation," *Mathematical and Computational Applications*, vol. 31, no. 4, art. 162, 2026. doi:10.3390/mca31040162.

[19] S. Poordastan, A. Askari Hemmat, and H. Saeedi, "A novel fractional Vieta-Lucas wavelet-based projection method for solving fractional delay differential equations," *Journal of Nonlinear Mathematical Physics*, published online 5 September 2026. doi:10.1007/s44198-026-00468-9.

[20] C. Jamilla, R. Mendoza, and I. Mező, "Solutions of neutral delay differential equations using a generalized Lambert W function," *Applied Mathematics and Computation*, vol. 382, art. 125334, 2020. doi:10.1016/j.amc.2020.125334.

[21] J. Čermák, T. Kisela, and L. Nechvátal, "The Lambert function method in qualitative analysis of fractional delay differential equations," *Fractional Calculus and Applied Analysis*, vol. 26, pp. 1545-1565, 2023. doi:10.1007/s13540-023-00176-x.